Received: 19 July 2021 | Revised: 16 September 2021 | Accepted: 8 October 2021

DOI: 10.1111/jace.18179

Journal of the American Ceramic Society

RESEARCH ARTICLE

Apatite and garnet stability in the Al–Ca–Mg–Si–(Gd/Y/Yb)–O systems and implications for T/EBC: CMAS reactions

Eeshani Godbole[1] | **Anette von der Handt**[2] | **David Poerschke**[1]

[1] Department of Chemical Engineering and Materials Science, University of Minnesota, Minneapolis, MN, United States

[2] Department of Earth Sciences, University of Minnesota, Minneapolis, MN, United States

Correspondence
Eeshani Godbole, Department of Chemical Engineering and Materials Science, University of Minnesota, Minneapolis, MN, United States.
Email: godbo043@umn.edu

Abstract

This work advances the understanding of the influence of rare earth (RE) ion radius on the stability and extent of the garnet solid solution phase in the (ytterbia/yttria/gadolinia)-calcia-magnesia-alumina-silica systems. Guided by the crystal chemistry and charge neutrality constraints, selected compositions in the notional garnet stability field were synthesized, equilibrated at 1400°C, and characterized to determine the equilibrium phases and their compositions. The results show a significant reduction in the stability of the silicate garnet relative to apatite with increasing RE ion radius. Apatite was not observed for any composition in the Yb-containing system, the Y-containing system formed both garnet and apatite, and there was no evidence of silicate garnets in the Gd-containing system. However, despite the apparent differences in stability relative to apatite, the extent of the garnet solid solution increases only slightly for the Yb- compared to Y-containing systems. The quantitative microchemical analysis suggests that Mg^{2+} prefers the octahedral site over the dodecahedral site in the garnet structure, and that the solubility of Mg^{2+} in the dodecahedral site increased in the system containing Yb^{3+} compared to Y^{3+}. The results are discussed for their relevance to reactions between RE-containing thermal and environmental barrier coatings and CMAS-type silicate deposits.

KEYWORDS

apatite, CMAS, environmental barrier coatings (EBC), garnet, rare earth, thermal barrier coatings (TBC)

1 | INTRODUCTION

Developing thermal and environmental barrier coating (T/EBC) materials and architectures to resist the degradation caused by ingested debris including volcanic ash, sand, and dust is critical to enable future turbine engine designs. At high temperatures within the engines, the debris adheres to component surfaces forming silicious deposits with varying concentrations of calcia, magnesia, alumina, iron oxide, and other minor components. These deposits, typically abbreviated CMAS (or CMFAS) based on the constituent oxides, dissolve and react with the T/EBCs.[1–6] Reactions forming crystalline products that consume large fractions of the molten deposit are desired to limit ingress of the melt into the strain tolerant microstructure of TBCs.[7] The same reaction products, however, can increase the CTE mismatch and thermocyclic stresses in dense EBCs.[8] The identity of the reaction

TABLE 1 Typical cationic site occupancies in apatite and garnet phases formed in T/EBC-CMAS interactions. Cations listed in parenthesis are beyond the scope of the current investigation

Phase	"A" site	"B" site	"T" site
Apatite: $[A_2B_8(TO_4)_6O_2]$	RE^{3+}, Ca^{2+}, Mg^{2+}	RE^{3+}, (Zr^{4+})	Si^{4+}
Garnet $[A_3B_2T_3O_{12}]$	RE^{3+}, Ca^{2+}, Mg^{2+}, (Fe^{2+})	Mg^{2+}, Al^{3+}, $(Fe^{3+}, Ti^{4+}, Zr^{4+})$	Al^{3+}, Si^{4+}, (Fe^{3+})

products depends on the coating and deposit compositions and reaction temperature. Understanding these reaction equilibria is important to design coatings that are robust against CMAS attack at increased turbine operating temperatures.

The calcium rare earth (RE) silicate apatite phase is an important crystalline reaction product. Its formation was initially observed in interactions between RE-oxide-containing coatings and silicate deposits.[6,7,9–12] Subsequently, its stability and composition range in CaO-SiO_2-$REO_{1.5}$ ternary systems[13–16] and its phase equilibrium with multicomponent CMAS type melts have been studied.[14,17,18] There is growing evidence that RE-containing aluminosilicate garnets are also an important reaction product. The garnet phase can incorporate a variety of cations from both the deposit and the coating material (Al^{3+}, Ca^{2+}, $Fe^{2+/3+}$, Mg^{2+}, RE^{3+}, Si^{4+}, Ti^{4+}, Zr^{4+}, etc.), and has been observed to form alongside or instead of apatite.[6,12,14,19–31] Unlike apatite, there is limited systematic understanding about the factors influencing the stability or compositional extent of the garnet phase. This work addresses the need by providing new insights into the effect of the RE cation size on the extent of the garnet phase and the relative stability of garnet and apatite.

Garnet has a cubic structure (space group $Ia\bar{3}d$) and its stoichiometry is represented by $A_3B_2T_3O_{12}$ where "A," "B," and "T" denote three crystallographic sites coordinated by 8, 6, and 4 oxygen anions, respectively. The wide range in the sizes of the coordination polyhedral allows a variety of cations to substitute into the structure, enabling extended solid solutions. Typical site occupancies determined using Pauling's rules and observations about the endmembers in geologic systems are shown in Table 1. Apatite has a hexagonal crystal structure (space group $P6_3/m$) and its stoichiometry is represented by $A_4B_6(TO_4)_6O_2$ where the *A* and *B* cations are coordinated by 9 and 7 oxygens, respectively. For silicate apatites, in which the tetrahedral *T* site is occupied by Si^{4+}, the similarity in the size of the *A* and *B* sites limits the variety of cation substitutions. The solid solution range is limited primarily to Ca^{2+}, Mg^{2+}, and Zr^{4+} substitution for RE^{3+}, with anion and cation vacancies providing charge compensation.[13,15,32] $Ca_2RE_8(SiO_4)_6O_2$ (where $A_4 = Ca_2RE_2$ and $B_6 = RE_6$) represents the defect-free stoichiometry and is the composition most-often observed in the context of CMAS-T/EBC interactions.

Coating materials containing $YbO_{1.5}$ and $YO_{1.5}$ show a greater propensity to form garnet upon reaction with CMAS deposits compared to those containing the larger RE cations, for example, $GdO_{1.5}$ or $NdO_{1.5}$, where silicate apatite is found more frequently.[6,12] Garnet is also favored in the presence of higher concentrations of aluminum, magnesium, and iron oxides, while titanium-rich deposits have stabilized kimzeyite-type garnets.[6,12,14,19–22,24–31] This behavior can be rationalized by the need to have a combination of large, intermediate, and small cation sizes to fill the three distinct sites. Likewise, coatings based on or containing rare earth aluminates are likely to cause a shift in reaction equilibria toward garnet formation.[33] Garnet is observed less frequently as an equilibrium reaction product at higher temperatures, and in some cases has been observed to grow on cooling rather than at temperature.[26,29,34]

Initial insight into the relative stability of apatite and garnet is gained by examining the endmembers $RE_{9.33}(SiO_4)_6O$ (the apatite terminus in the $REO_{1.5}$-SiO_2 binary), $Ca_2RE_8(SiO_4)_6O_2$ (the vacancy-free nominal apatite stoichiometry), and $RE_3Al_5O_{12}$ (the rare earth aluminate garnet, RE-AG). These have been studied in a variety of contexts including nuclear waste immobilization,[35] solid oxide fuel cells and sensors, phosphors, and laser technology,[36–39] and for their petrologic and geochronologic importance.[40,41] Data from the $REO_{1.5}$-SiO_2[42–45] and $AlO_{1.5}$-$REO_{1.5}$[34,46–56] binary systems, studies into apatite crystal chemistry[13,15,35,36,57,58] for calcium-containing rare earth apatite stability, and the literature on T/EBC-CMAS interactions[6,7,12,18] were used to infer the stability of the endmembers at 1400°C. The results are plotted in Figure 1 as a function of the 8-fold coordinated RE ion radii.[59] With increasing RE ion radius, the stability of the Ca-free apatite increases while that of the pure aluminate garnet endmember decreases. The Ca-containing apatite endmember is stable for most RE oxides, but RE cation partition coefficients in geological samples suggest a preference for the RE to enter the garnet phase for the smaller RE cations.[12] These observations hint at a strong dependence of the rare earth ion radius on the stability of apatite and garnet phases. The transition in their relative stability appears to occur over the RE cation size range encompassing Yb^{3+}, Y^{3+}, and Gd^{3+}, which are selected as the focus for the present investigation.

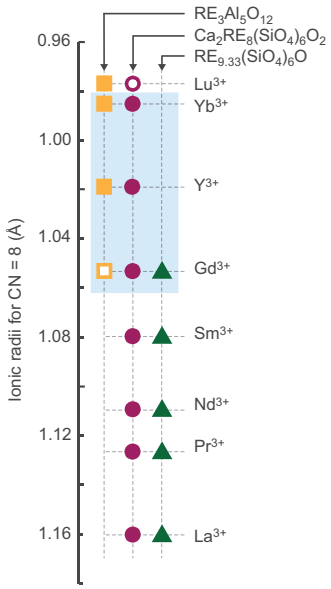

FIGURE 1 Stability of silicate apatite and aluminate garnets at 1400°C as a function of RE cation radius. Filled symbols indicate that the phase is stable, open symbols indicate inconsistent evidence in the literature, and the absence of the symbol indicates that the phase is not reported to be stable

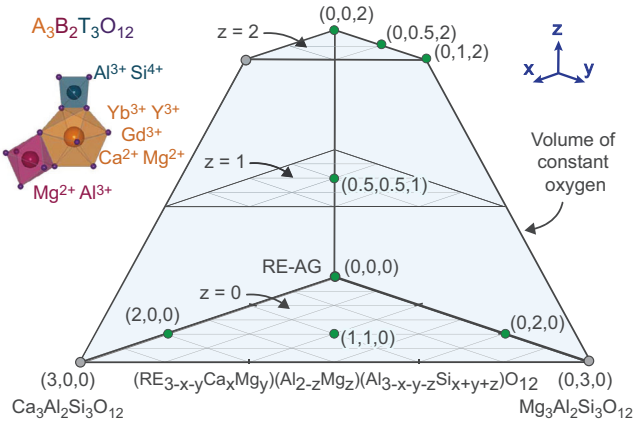

FIGURE 2 Theoretical composition extent for garnet stability in the RE-CMAS system. Sample compositions studied in the Y, Yb, and Gd-CMAS systems are indicated. Adapted from ref. 23

In prior work,[23] crystal chemistry and charge neutrality constraints were utilized to specify the theoretical extent of the garnet phase field in the RE+CMAS system (Figure 2). That study, which focused on the Y-CMAS system, found no evidence that vacancies or interstitials play a significant role in facilitating cation substitutions. The concentration of iron oxide in the reaction mixture has a significant impact on the identity and composition of the crystalline products formed during coating-deposit interactions. Iron can exist in two possible valence states and as shown in Table 1, allowing iron to occupy all three cationic sites in the garnet structure. The complexity brought forth by these factors would obscure insights into the influence of other major ions present in CMAS on the stability and extent of the garnet phase field. Therefore, this report is restricted to the Gd/Y/Yb+CMAS system, which provides a foundation for future analysis of the effect of iron oxide on garnet phase equilibria.

Using the pure RE aluminate garnet end member (RE-AG) as the starting point, the garnet stoichiometry is given by $(RE_{3-x-y}Ca_xMg_y)(Al_{2-z}Mg_z)(Al_{3-x-y-z}Si_{x+y+z})O_{12}$. Stoichiometries are abbreviated as *RE-(x,y,z)* where RE denotes the rare earth cation, x and y represent Ca^{2+} and Mg^{2+} substitution, respectively, for RE^{3+} in the *A* site and z represents the substitution of Mg^{2+} for Al^{3+} in the B site. The crystal chemistry constrains the substitutions to $0 \le z \le 2$ and $x + y + z \le 3$.

The present work expands on the investigation of the Y+CMAS quinary system at 1400°C[23] to understand the behavior of Yb^{3+} and Gd^{3+}. In addition to falling near the apatite to garnet transition in the endmembers (Figure 1), these three cations are arguably the most important for state-of-the-art TBC and EBC compositions. The key questions addressed in this study pertaining to the stability of the silicate garnet and silicate apatite phases in the RE+CMAS system are:

a. How significant is the influence of the RE ion radius on the compositional extent of garnet phase given that Yb^{3+} is roughly 3% smaller and Gd^{3+} is roughly 3% larger than Y^{3+} in the eightfold coordination site of the garnet crystal structure?
b. To what degree do structural distortions caused by changes in the RE cation size affect the solubilities and partitioning of other cations in the different cationic sites of silicate garnets?
c. How does the rare earth ion radius influence the relative stability of the garnet and apatite?
d. How do the Ca^{2+}: Si^{4+} ratios and the concentration of Al^{3+} influence the equilibria between apatite and garnet?

2 | EXPERIMENTAL METHODS

2.1 | Compositions studied

The compositions selected to study garnet stability in the Yb- and Gd-CMAS systems (Table 2) delineate the boundary of the aluminosilicate garnet phase field in the Y-CMAS system at 1400°C. As elaborated below, these compositions proved sufficient to understand the relevant equilibria in both systems. Most of the chosen compositions contain 25 mol% SiO_2 ($x + y + z = 2$), with varying

TABLE 2 Summary synthesized compositions with expanded nominal stoichiometries

ID	Coordinate	Composition (mol%)					Stoichiometry*
		CaO	MgO	$AlO_{1.5}$	SiO_2	$REO_{1.5}$	
1	RE-(0,0,0)	0	0	62.5	0	37.5	$(RE_3)(Al_2)(Al_3)O_{12}$
2	RE-(2,0,0)	25	0	37.5	25	12.5	$(RECa_2)(Al_2)(AlSi_2)O_{12}$
3	RE-(0,2,0)	0	25	37.5	25	12.5	$(REMg_2)(Al_2)(AlSi_2)O_{12}$
4	RE-(1,1,0)	12.5	12.5	37.5	25	12.5	$(RECaMg)(Al_2)(AlSi_2)O_{12}$
5	RE-(0.5,0.5,1)	6.25	18.75	25	25	25	$(RE_2Ca_{0.5}Mg_{0.5})(AlMg)(AlSi_2)O_{12}$
6	RE-(0,0,2)	0	25	12.5	25	37.5	$(RE_3)(Mg_2)(AlSi_2)O_{12}$
7	RE-(0,0.5,2)	0	31.25	6.25	31.25	31.25	$(RE_{2.5}Mg_{0.5})(Mg_2)(Al_{0.5}Si_{2.5})O_{12}$
8	RE-(0,1,2)	0	37.5	0	37.5	25	$(RE_2Mg)(Mg_2)(Si_3)O_{12}$

*This is the theoretical stoichiometry if garnet was the single equilibrium phase. In reality, this stoichiometry is not observed except in the case of the pure aluminate endmember (ID = 1).

TABLE 3 Abbreviations used for phases observed at equilibrium and the formulae for endmembers

Phase name	Stoichiometry	Abbreviation
Alumina	Al_2O_3	Al
Apatite	$(Ca,Mg)_2RE_8Si_6O_{26}$	Ap
Garnet	$A_3B_2T_3O_{12}$	G
Liquid (glass)		L
Melilite (Gehlenite)	$Ca_2Al_2SiO_7$	Mel
Olivine	Mg_2SiO_4	Oli
Spinel	$MgAl_2O_4$	Sp
Ytterbium disilicate	$Yb_2Si_2O_7$	YbDS
Ytterbium monosilicate	Yb_2SiO_5	YbMS
Yttrium disilicate	$Y_2Si_2O_7$	YDS
Yttrium monosilicate	Y_2SiO_5	YMS
Gadolinium aluminum perovskite	$GdAlO_3$	GdAP

concentrations of the other cations. Two additional MgO-rich compositions were studied to elucidate the influence of Mg^{2+} on apatite and garnet stability. The pure aluminate garnet endmembers $Yb_3Al_2Al_3O_{12}$ and $Gd_3Al_2Al_3O_{12}$ were synthesized and studied to confirm their stability at 1400°C. Additional analysis of some samples generated as part of the prior Y-CMAS study[23] was also performed.

2.2 | Synthesis and heat treatment

Compositions were synthesized using reverse coprecipitation, wherein stoichiometric ratios of calibrated precursor solutions were added to the precipitant in a dropwise manner. Solutions of tetraethyl orthosilicate (TEOS) and nitrates of aluminum, calcium, gadolinium, magnesium, and ytterbium (Alfa Aesar, >99.9% purity on a metal basis) in 200 proof ethanol, were first calibrated to attain their oxide yield. Ammonium hydroxide (28-30%, ACS grade, Fisher Chemicals) or, for calcium-containing stoichiometries, a mixture of ammonium hydroxide and ammonium carbonate (analysis grade, ACROS Organics), were used as precipitants. The pH of the mixture was maintained above 10 during the coprecipitation reaction. The precipitates were washed with 200 proof ethanol then calcined at 1000°C. The resulting mixed oxide powders were pressed into 6 mm diameter pellets, equilibrated at 1400°C for 100 h in air, and were quenched by extraction from the hot furnace.

2.3 | Characterization and stoichiometry assignment for garnet and apatite

Each of the heat-treated pellets was cut into two portions. One half was prepared for microstructure analysis and the other was crushed in an alumina mortar and pestle for powder X-ray diffraction analysis (XRD, Rigaku Miniflex 600, 10° to 70° 2θ, 30 min scan). Samples showing melt formation were mounted in epoxy and polished using diamond suspensions to attain a 1 μm finish. The sub-solidus samples were polished using diamond lapping films, thermally etched at 1400°C for 3 h, and quenched.

Backscattered scanning electron microscopy (BSE SEM, Hitachi SU8230) was performed with contrast-brightness settings selected to highlight the different phases. Semi-quantitative energy dispersive spectroscopy (EDS, Thermo Noran System 7) data was used for preliminary phase identification in the SEM. Quantitative chemical analysis was performed by electron probe microanalysis with wavelength dispersive spectroscopy (EPMA-WDS, JEOL JXA-8530FPlus) using a 30 nA beam current with 10 kV accelerating voltage and a focused beam diameter. Appropriate interference corrections were applied for X-ray lines where necessary. Data were acquired using the PETL

TABLE 4 Summary of equilibrium phase assemblages for compositions under study in the Gd/Y/Yb+CMAS systems and equilibrium garnet stoichiometries for the Yb system based on EPMA measurements

ID	Coordinate	Observed Phase List			Equilibrium garnet stoichiometry in the Yb+CMAS system
		Yb	Y	Gd	
1	RE-(0,0,0)	G	G	G,GdAP,Al	$(Yb_{2.99})(Al_{1.99})(Al_{3.00})O_{11.98}$
2	RE-(2,0,0)	G, L	G, L	Ap, L, Mel	$(Yb_{2.11}Ca_{0.92})(Al_{1.97})(Al_{2.04}Si_{0.96})O_{12.02}$
3	RE-(0,2,0)	G, Sp, L	G, Sp, L	Sp, L	$(Yb_{2.04}Mg_{0.96})(Al_{1.53}Mg_{0.47})(Al_{1.49}Si_{1.51})O_{12.04}$
4	RE-(1,1,0)	G, Sp, L	G, Sp, L	Ap, Sp, L	$(Yb_{2.14}Ca_{0.54}Mg_{0.32})(Al_{1.68}Mg_{0.32})(Al_{1.80}Si_{1.20})O_{12.01}$
5	RE-(0.5,0.5,1)	G, L	G, Sp, Ap, L	Ap, Sp, L	$(Yb_{2.22}Ca_{0.42}Mg_{0.36})(Al_{0.90}Mg_{1.10})(Al_{1.04}Si_{1.95})O_{12.03}$
6	RE-(0,0,2)	G, YbMS	G, YMS	Ap, Oli	$(Yb_{2.76}Mg_{0.24})(Al_{0.23}Mg_{1.76})(Al_{0.89}Si_{2.11})O_{12.05}$
7	RE-(0,0.5,2)	G, YbMS,YbDS, Oli	G, Oli, Ap, L	Ap, Oli, L	$(Yb_{2.34}Mg_{0.66})(Al_{0.13}Mg_{1.87})(Al_{0.38}Si_{2.62})O_{12.04}$
8	RE-(0,1,2)	YbMS,YbDS,Oli	Oli, Ap, YDS	Ap, L, Oli	N/A

crystal for Ca-K_α, TAPL for Al-K_α, Yb-M_α and Gd-M_α, TAP for Mg-K_α and Si-K_α, and LiFL for Yb-K_α and Gd-K_α. $YbPO_4$ (NMNH 168498, National Museum of Natural History), GGG (MAC Gadolinium Gallium Garnet), $GdPO_4$ (NMNH 168488), anorthite (NMNH 137041), spinel (Taylor, $MgAl_2O_4$), YAG (MAC $Y_3Al_5O_{12}$), forsterite (George Rossman, Mg_2SiO_4), and diopside (Taylor, $CaMgSi_2O_6$) were used as standards. Line compounds YbAG ($Yb_3Al_2Al_3O_{12}$) and GdAG ($Gd_3Al_2Al_3O_{12}$) observed in the samples under study were also used as secondary standards for the analyses.

Quantitative chemical analysis using EPMA was performed on ~10 grains for solid solution phases and ~5 grains for line compounds. The line compounds were used as internal standards to cross-check the analysis; their measured stoichiometries were generally within ±1 at percentage of their expected stoichiometry. Analysis spots were placed at the center of large grains and glass pools. Glass stoichiometries were confirmed by using spots near and far from crystalline regions.

3 | RESULTS

The equilibrium phases identified based on the XRD analysis and microstructural and chemical data from SEM-EDS and EPMA analyses are summarized in Table 4 using the abbreviations listed in Table 3. Representative micrographs and XRD plots are shown in Figure 3.

3.1 | Equilibrium relationships in the Yb+CMAS system

3.1.1 | Overall phase equilibria

The primary observations about the equilibria in the Yb+CMAS system are:

a. Seven of the eight compositions form garnet phase at 1400°C. The equilibrium garnet stoichiometries inferred from the EPMA data are reported in Table 4. The only composition that did not form garnet had greater silica content, that is, $x + y + z \geq 2$.
b. The apatite phase was not observed in any of the Yb-CMAS samples
c. Half of the samples stayed below the solidus and the other half showed melt formation
d. Most of the compositions containing MgO formed spinel or olivine in equilibrium with the other phases. Those with a comparatively higher MgO concentration formed olivine.
e. The aluminate end member ((0,0,0) - $Yb_3Al_2Al_3O_{12}$) formed essentially single-phase garnet; scattered grains of a Yb-rich phase suggest a small deviation of the synthesized composition from the intended bulk stoichiometry.

3.1.2 | Extent of the garnet phase field in Ca free samples

Figure 4 shows the equilibrium garnet stoichiometries corresponding to the four calcium-free samples plotted on the y - z ($x = 0$) plane of Figure 2. This analysis indicates that Mg^{2+} ions occupy both the A and B sites in Yb containing silicate garnets. The equilibrium garnet stoichiometry formed in sample Yb-(0,2,0) shows an upward, leftward diagonal shift away from the nominal stoichiometry. This indicates a preference for Mg^{2+} to partition into the B site versus the A site. This conclusion is further supported by the smaller relative shift in the opposite direction for samples Yb-(0,0,2) and Yb-(0,0.5,2) in which the B site is fully occupied by Mg^{2+} in the notional formula. In those samples, the equilibrium garnet compositions show a slight decrease in the Mg^{2+} concentration of the B site as it partitions into the A site.

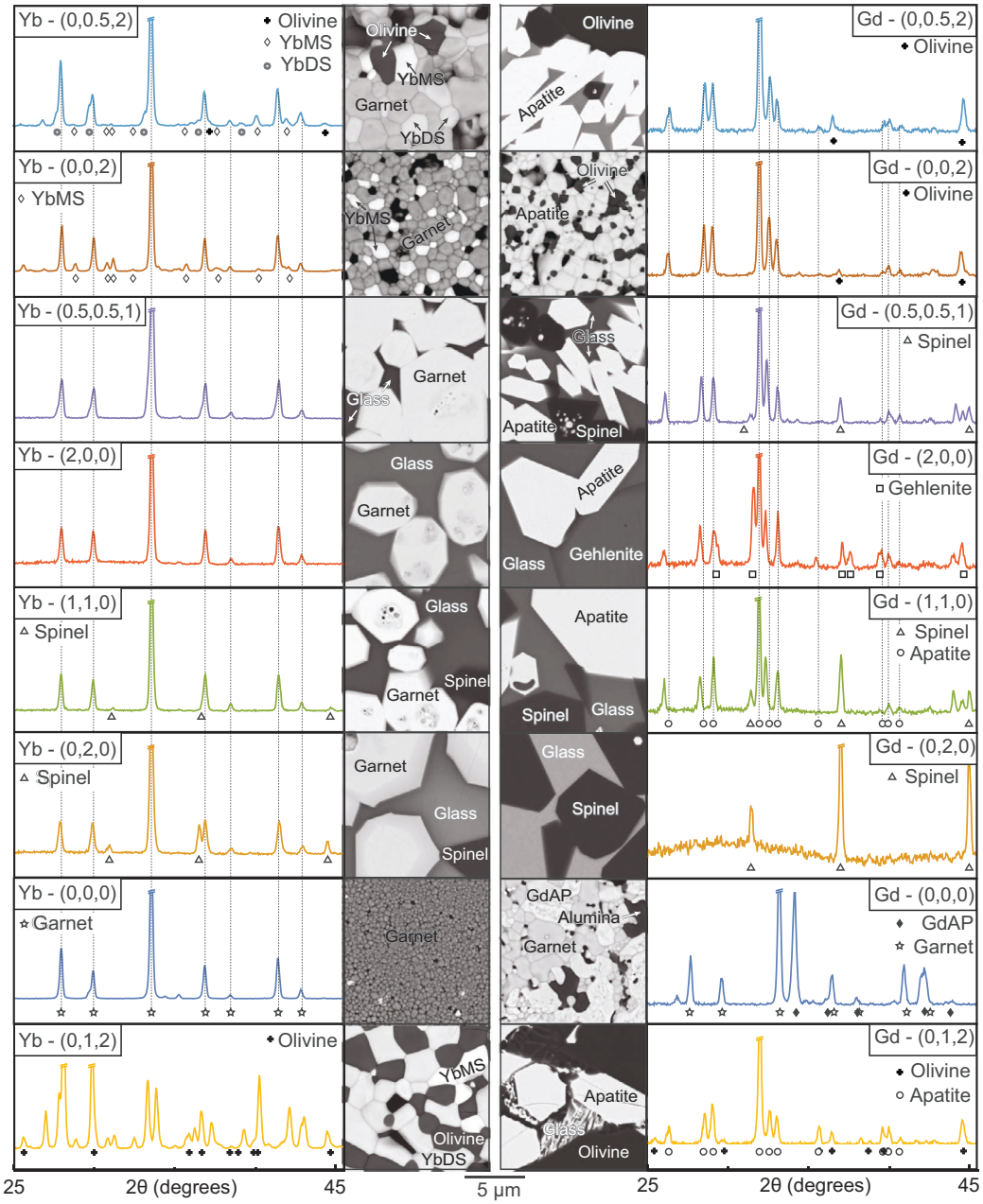

FIGURE 3 XRD plots and BSE micrographs depicting equilibrium phase assemblages for compositions studied in the Yb and Gd + CMAS systems. All XRD data was normalized to the strongest reflection and line breaks (//) represent peaks with intensities extending beyond the scale

3.1.3 | Extent of the garnet phase field in samples containing CaO and MgO

Figure 5 shows projections of equilibrium garnet stoichiometries onto the $x - y$ ($z = 0$) plane of the theoretical garnet extent. The influence of cation partitioning in the A site on the extent of the garnet phase field can be inferred from this projection. The equilibrium garnet compositions formed in the Yb-(0.5,0.5,1) and Yb-(1,1,0) samples, which have equal concentrations of Ca^{2+} and Mg^{2+} in the A site in the nominal stoichiometries, show a small deviation towards the Ca^{2+} axis ($y = 0$) from the central axis of the $z = 0$ plane. This indicates a slight preference for the larger Ca^{2+} (vs. the smaller Mg^{2+}) in the A site.

3.1.4 | Silica solubility in the Yb-CMAS garnets

Figure 6A shows the relationship between the concentration of silicon and the total alkaline earth (AE) cation (calcium + magnesium) concentration in the equilibrium

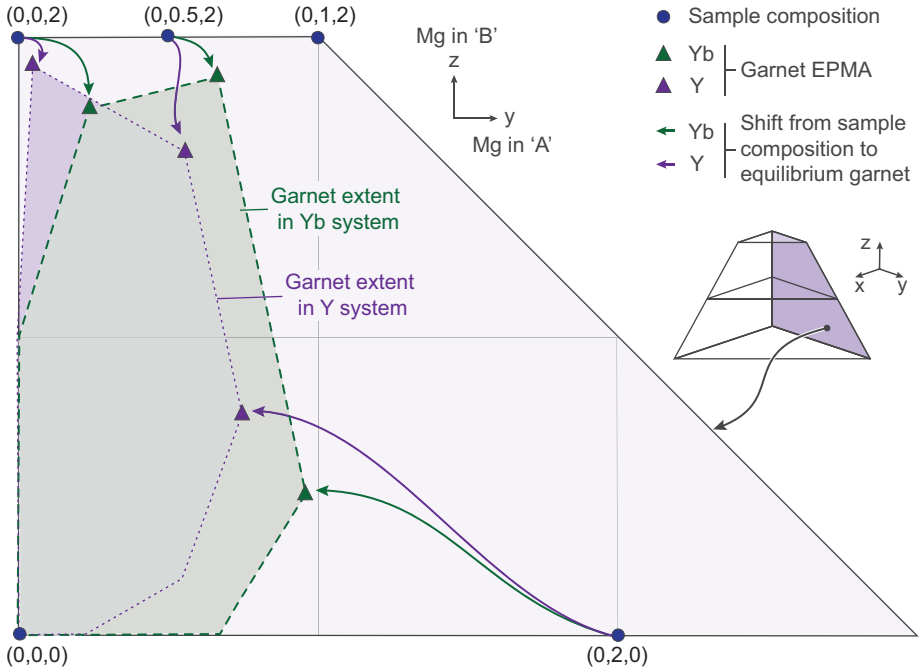

FIGURE 4 Sample compositions and equilibrium garnet stoichiometries of the Ca-free samples plotted on the y-z plane. Yb data from this study overlaid on results from the Y+CMAS system.[23] The equilibrium garnet stoichiometries were used to determine the extent of the garnet solid solution field at 1400°C. In both systems, the Mg^{2+} solubility is greater in the B site vs. the A site. The Mg^{2+} solubility limit in the A site for the Yb garnets slightly higher than for the Y garnets

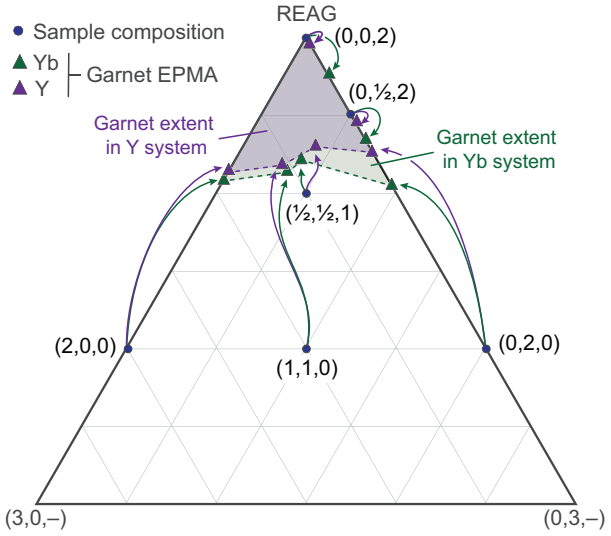

FIGURE 5 Projections of synthesized stoichiometries and equilibrium garnet stoichiometries on the z = 0 plane of Figure 2 for the Yb+CMAS and Y+CMAS[23] systems. The extent of the garnet phase field in the Yb+CMAS system extends to slightly higher MgO compositions than the Y+CMAS system

garnet. The garnet crystal chemistry and charge neutrality constraints dictate that these values should be equal (i.e Si = *x+y+z in the chemical stoichiometry*) and fall along the dashed line. The results are consistent with these constraints within the uncertainty bounds of the chemical analysis.

Figure 6B shows the equilibrium silica solubility limit as a function of the AE concentration in the sample overall. Values falling below a one-to-one relationship indicate that SiO_2 preferentially partitions into equilibrium phases other than garnet. Based on data from the samples analyzed, the maximum solubility of Si^{4+} in the Yb + CMAS garnet at 1400°C is 33 cat%. This corresponds to an equilibrium garnet composition of $(Yb_{2.34}Mg_{0.66})(Al_{0.13}Mg_{1.87})(Al_{0.38}Si_{2.62})O_{12.10}$, formed by the Yb-(0,0.5,2) sample. This limit, which corresponds to ~90 % of the maximum SiO_2 solubility limit defined by the crystal chemistry, is considerably higher than the maximum in the Y-containing system.

3.2 | Phase equilibrium relationships in the Gd+CMAS system

Key observations about the equilibria in the Gd+CMAS system include:

a. The garnet phase was only observed for Gd-(0,0,0), the pure aluminate endmember. Garnet was not formed in any of the silica-containing samples.
b. Every sample except Gd-(0,0,0) and Gd-(0,2,0) formed apatite (Table 5). For samples containing both Ca and Mg ions, the apatite contained significantly more Ca^{2+} than Mg^{2+}. Silicate apatites closely aligned

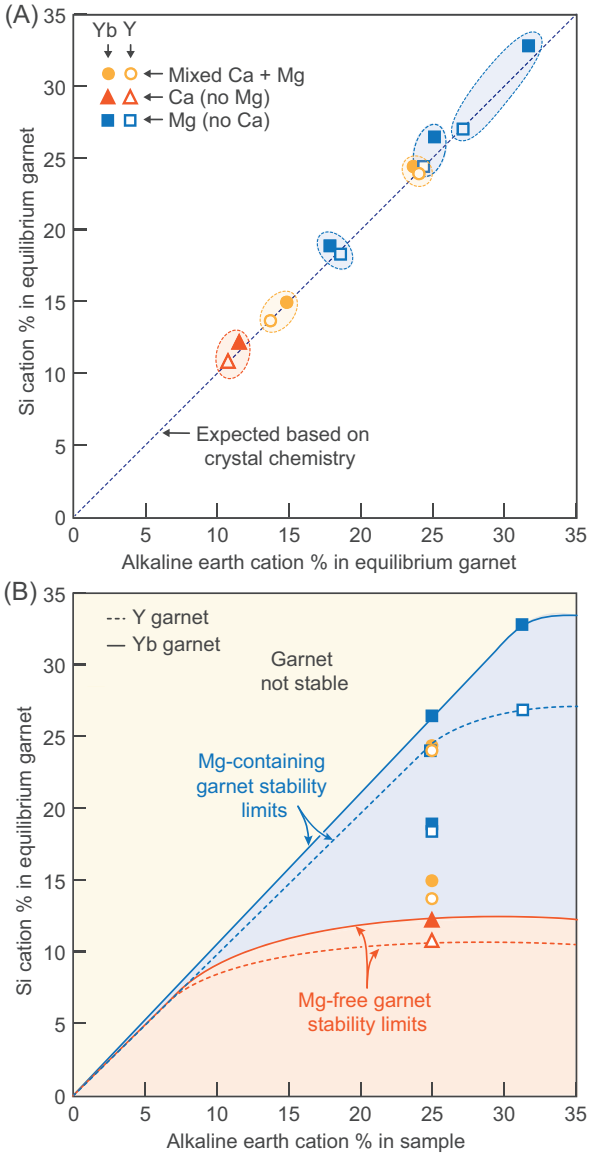

FIGURE 6 (A) A direct correspondence between the total alkaline earth concentration and measured Si^{4+} content in equilibrium garnets follows the stoichiometry dictated by chemistry and charge neutrality constraints. The Si^{4+} solubility in Yb garnets is higher than that of Y garnets. (B) The presence of Mg^{2+} enhances garnet Si^{4+} solubility in both Y and Yb systems. Uncertainty estimates are comparable to the symbol size

with the nominal stoichiometries of $Ca_2RE_8Si_6O_{26}$ or $Mg_2RE_8Si_6O_{26}$ for samples containing only Ca^{2+} or only Mg^{2+} as the AE ions.

c. Six of the eight samples partially melted at 1400°C. In most cases, the liquid was quenched as a glass, but Gd-(0,1,2) showed fine crystallites in the melt pools (Figure 3).
d. All the magnesium-containing samples formed either spinel or olivine at equilibrium.

4 | DISCUSSION

4.1 | Garnet stability and solid solution extent in Yb-, Y-, and Gd+CMAS systems

4.1.1 | Observations at 1400°C

Generally, the Yb+CMAS system followed trends similar to those in the Y+CMAS system. Starting with the aluminate endmember, the garnet stability decreases with increasing calcium and magnesium substitution for ytterbium (and a concomitant increase in silica content). Additionally, the fraction of liquid formed at equilibrium increases as the Yb content decreases. The secondary phases in the Yb+CMAS system include spinel and olivine in the Mg^{2+}-containing systems and ytterbium mono- and di-silicates. These assemblages are consistent with the apparent inability of the garnet structure to fully accommodate the Ca^{2+}, Mg^{2+}, and Si^{4+} in the silica-rich sample compositions.

Figure 5 shows the projection of equilibrium garnet stoichiometries in the Y- and Yb+CMAS systems onto the $z = 0$ plane, providing an additional comparison of the extent of the garnet solid solution in the Y- and Yb+CMAS systems. The garnet phase field in the Yb+CMAS system extends to slightly greater AE content than that in the Y+CMAS system; this increase is more pronounced in compositions containing Mg^{2+}. In the presence of Yb^{3+}, both Ca^{2+} and Mg^{2+} have comparable solubilities of about 12 cat% in the A site whereas the solubility of Mg^{2+} in the

TABLE 5 Equilibrium apatite stoichiometries for the Gd systems measured by EPMA

ID	Sample	Composition				
		CaO	MgO	$AlO_{1.5}$	SiO_2	$GdO_{1.5}$
2	Gd-(2,0,0)	13.2	–	0.4	37.3	49.0
4	Gd-(1,1,0)	12.4	0.4	0.2	37.4	49.7
5	Gd-(0.5,0.5,1)	9.9	2.8	0.2	37.4	49.9
6	Gd-(0,0,2)	–	9.0	4.3	33.6	53.1
7	Gd-(0,0.5,2)	–	12.2	0.6	36.7	50.5
8	Gd-(0,1,2)	–	12.5	–	37.5	50.1

A site is slightly lower at 9 cat% in presence of Y^{3+}. Furthermore, Yb^{3+}-containing equilibrium garnets show very marginal shifts in the same direction away from the nominal stoichiometries containing both CaO and MgO, for example, Yb-(1,1,0) and Yb-(0.5,0.5,1). In case of the Y^{3+} system however, the relative concentrations of the AE ion in the nominal stoichiometry appeared to influence the equilibrium garnet shifts toward either the Ca axis ($y = 0$) or the Mg axis ($x = 0$). These observations suggest a slightly higher Mg^{2+} stability in the A site in presence of Yb^{3+} ions than Y^{3+} ions. However, the results also indicate that differences in the relative stability of garnet in the Y- versus Yb-systems (elaborated below) are more likely due to changes in the intrinsic stability relative to other phases, rather than differences in the extent of the garnet field.

In the Gd+CMAS system, garnet was only observed for the Gd-(0,0,0) sample corresponding to the aluminate garnet endmember ($Gd_3Al_2Al_3O_{12}$, GdAG). The implication is that the presence of SiO_2 sufficiently destabilizes the garnet structure (or stabilizes other Gd-containing phases such as apatite) to limit Si^{4+}, Mg^{2+}, and Ca^{2+} solubility in GdAG at equilibrium. The RE mono- and di-silicate phases are absent in the Gd+CMAS systems, presumably replaced by the silicate apatite phase as the sink for gadolinia. Olivine and spinel are also important secondary phases that consume the excess magnesia and alumina that are not readily accommodated in the apatite. Notably, in contradiction to the Gibbs phase rule, the Gd-(0,0,0) sample contained three phases, namely alumina, GdAP ($GdAlO_3$), and GdAG, rather than forming single-phase garnet. This observation is consistent with the mixed reports in the literature sources about whether GdAG is stable as a single phase at 1400°C, or if Al_2O_3 + GdAP is the equilibrium assemblage.[34,54–56] Shorter (25 h) and longer (500 h) 1400°C heat treatments for the Gd-(0,0,0) sample produced equivalent phase assemblages and similar grain size distributions to the 100 h heat treatment. No cooling effects were noted for any of the heat-treated samples. Further investigations into this issue are beyond the present scope of this study. A comparative summary of the microstructures seen for the three heat treatments of the Gd-(0,0,0) sample have been reported in Figure S4. The results are insufficient to draw a definitive conclusion, and this issue remains under study.

4.1.2 | Literature observations and temperature effects

Garnet has been observed for a variety of T/EBC materials reacting with CMAS deposits over a range of temperatures. In conjunction with the results from this study, the literature data provide insights into the temperature-dependent changes in the garnet field extent. Figure 7 shows projections of equilibrium garnet stoichiometries for the Y+CMAS and Yb+CMAS systems reported for T/EBC+CMAS experiments at different temperatures.[14,19,21,26,29] The garnet compositions fall along the *x*-axis (the Ca-rich side of the system), which is likely due to the high CaO concentration in the CMAS, causing most Mg^{2+} to enter the B site. The CaO, MgO, and SiO_2 content in the equilibrium garnets increases for lower reaction temperatures. Using this limited temperature-dependent data along with the shape of the garnet field identified in ref. 23 and the current work, tentative isotherms are shown in Figure 7[a]. This

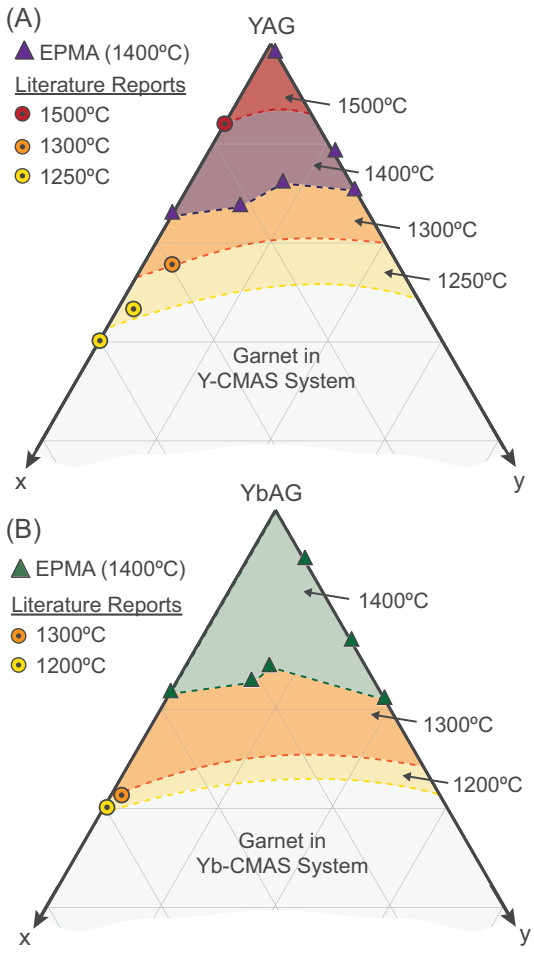

FIGURE 7 Equilibrium stoichiometries corresponding to garnets formed in the (A) Y+CMAS system at 1250°C,[26] 1300°C,[14] 1400°C,[23] and 1500°C[19] and the (B) Yb+CMAS system at 1200°C,[21] 1300°C,[29] and 1400°C (this work). Inferred temperature dependence on the extent of garnet stability is shown by the shaded regions

[a] Reported garnet compositions falling well outside the Yb- and Y+CMAS systems,[20,22,25,27,31] or for which the compositions didn't conform nominal formula,[12,24] aren't included in the figure but exhibit behavior consistent with the observed temperature-dependent trends.

result shows a considerable contraction in the field while increasing from 1200°C to 1500°C. The implication is that the effect of temperature on the extent of garnet phase field is greater than the effect of the change in cation size from Yb^{3+} to Y^{3+} even though the intrinsic stability is contingent on the rare earth ion present in the system.

4.2 | Influence of rare earth ions on cation partitioning in silicate garnets

The interconnected polyhedra in the garnet structure imply that substitutions in one site can distort adjacent sites. It is thus reasonable to expect that changing the RE cation radius will influence the nature of cation partitioning in the equilibrium garnets. The z versus y ($x = 0$) plane of the notional garnet stability range (Figure 4) provides information about the Mg^{2+} partitioning between the octahedral and dodecahedral sites for the Ca-free compositions. Comparison of the extent of the equilibrium garnet field for the Y- and Yb+CMAS systems shows that the Mg^{2+} is more readily accommodated in the octahedral 'B' site, as evidenced by the upward, leftward shift of the garnet composition formed by the (0,2,0) samples compared to the minimal downward shift for garnets formed in the (0,0,2) and (0,0.5,2) samples. However, the y values (corresponding to the Mg^{2+} content in the A site) for the Yb-containing garnets are higher than those for the Y-containing counterparts while some of the z values (corresponding to the Mg^{2+} content in the B site) shift lower. The inference is that the smaller difference between Mg^{2+} (0.89 Å) and Yb^{3+}(0.985 Å) versus Mg^{2+} and Y^{3+}(1.019 Å) allows higher Mg^{2+} solubility in the A site for the Yb-based system.

Figure 6A shows a direct correspondence between the silica content and the total AE content in garnet, consistent with the crystal chemistry and charge neutrality constraints. It also shows that although the Si^{4+} content is similar between equivalent Yb- and Y-garnets with intermediate AE content, the Yb-containing garnets dissolve more silica compared to the Y-garnets as the AE content increases. The maximum Si^{4+} solubility in Yb+CMAS garnet is 33 cat% observed in Yb-(0,0.5,2). This value is close to the maximum possible silica solubility (37.5 cat%) and is greater than the maximum solubility of 27 cat% Si^{4+} in the equivalent Y-(0,0.5,2) sample. The presence of Yb^{3+} thus appears to have increased the solubility of Mg^{2+} in the equilibrium garnet with a corresponding increase in the Si^{4+} solubility. Figure 6B shows that for the same total AE content in the nominal stoichiometries, Yb^{3+} containing garnets pull in more Si^{4+} at equilibrium. This increase in Si^{4+} solubility is more pronounced for compositions containing Mg^{2+} than those containing just Ca^{2+} as the AE ion.

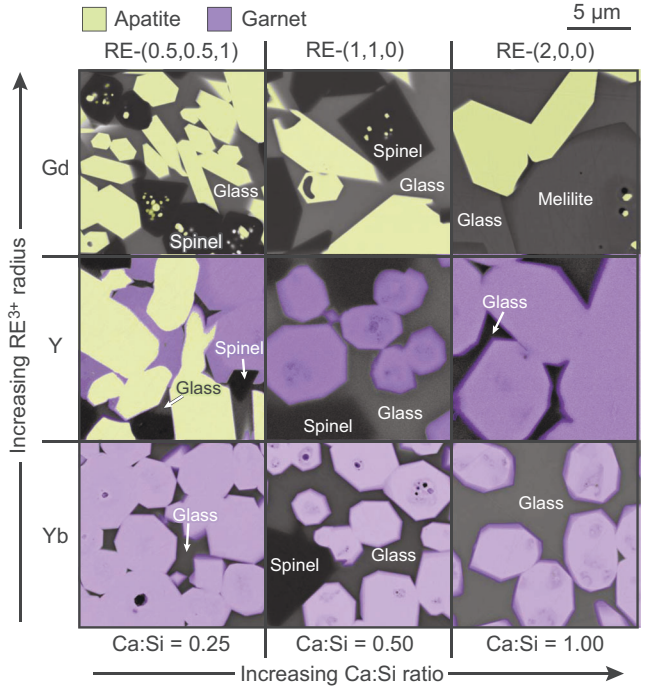

FIGURE 8 Equilibrium phase assemblages demonstrating the effect of RE^{3+} and Ca:Si ratio on apatite and garnet stability have been shown above. The garnet and apatite grains have been colored based on their relative BSE contrast

4.3 | Relative stability of apatite and garnet transitions and implications for T/EBC – CMFAS reactions

The results are consistent with the expectations that the apatite stability increases relative to garnet with increasing RE cation radius. Other factors that have been proposed to affect silicate apatite stability include the Ca:Si ratio and the alumina content in the reacting system.[6,12,14] The samples investigated in this study were analyzed to examine how these factors affect the transition in stability between apatite and garnet. Key trends are illustrated in Figures 8 and 9. In these figures, the apatite and garnet grains were identified and colored based on a combination of EDS, EPMA, and BSE data to aide in visualizing the distribution of the phases.

Figure 8 shows that for a constant Ca:Si ratio, the increase in RE^{3+} radius from Yb^{3+} to Y^{3+} to Gd^{3+} (up each column in Figure 8) leads to an increase in the amount of apatite relative to garnet. Additionally, in the Y+CMAS system, an increase in the Ca:Si ratio (left to right in each row in Figure 8) is accompanied by a decrease in apatite

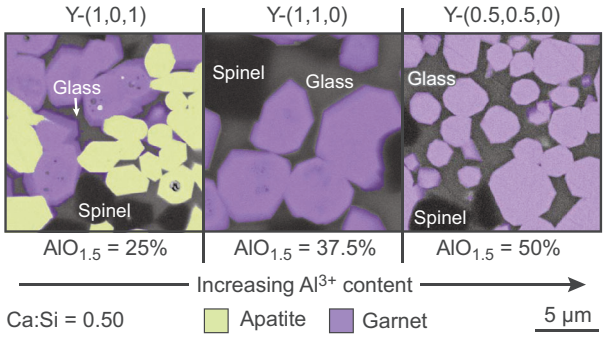

FIGURE 9 These micrographs demonstrate the effect of changing Al^{3+} content on apatite and garnet stability for a fixed Ca:Si ratio. The garnet and apatite grains were identified based on composition measurements and re-colored based on their relative BSE contrast

content. This is a counterintuitive result since increasing the Ca:Si ratio typically drives apatite formation. However, in this case, the Al^{3+} content is roughly twice that of the most-often studied CMAS compositions. Since Al^{3+} is necessary to stabilize garnet, the inference is that the greater Al^{3+} content pushes the equilibrium toward the garnet phase even though there is sufficient Ca^{2+} content to enable apatite formation. These results corroborate the inference that the garnet stability decreases and apatite stability increases with increasing RE radius, and is also heavily dependent on the Ca:Si ratio and Al^{3+} content.

The Gd+CMAS system formed apatite but never in equilibrium with garnet while compositions studied in the Yb+CMAS system formed garnet but never in equilibrium with apatite. However, several compositions in the Y+CMAS system showed the formation of apatite in equilibrium with garnet. This suggests that the Y^{3+} radius is favorable for the stability of both phases in equilibrium at higher temperatures. Additional insight comes from compositions studied in the Y+CMAS system with equivalent Ca:Si ratio (Figure 9), which show an increase in the garnet fraction and a decrease in apatite content with an increase in the $AlO_{1.5}$ concentration in the system. This confirms that in addition to the Ca:Si ratio, Al^{3+} content also plays a key role in influencing the apatite – garnet stability and equilibrium transitions.

Interactions of RE-based T/EBCs with CMAS results in the formation of various crystalline phases. The kinetics and morphology of apatite growth are known to be favorable to arrest melt penetration through the strain compliant morphology of TBCs.[4,26,31] This work reinforces the understanding that TBCs with larger RE ions are more likely to form apatite and less likely to form garnet. Compared with Y-containing coatings, reactions with Yb-containing coatings are more likely to form garnet, and the resulting garnet will have a higher solubility of Mg^{2+} and Si^{4+}, enabling them to consume more melt per mole of coating reacted. Furthermore, their formation depletes the melt of AE ions, increasing the residual melt viscosity.[14] In combination, these factors would be expected to better arrest melt infiltration in Yb-based TBCs. However, the slow nucleation and growth kinetics of garnet compared to apatite have been shown to limit the efficacy of garnet in CMAS attack mitigation, even though garnet crystallization consumes more moles of CMAS oxides than silicate apatite.[29] In EBC-CMAS interactions, it is desirable to minimize the reaction between CMAS and the coating to avoid the formation of products that increase the CTE mismatch with the substrate relative to the original coating. In that regard, garnet formation may be less desirable since a larger volume of crystalline product would form.

It is generally understood that Ca^{2+} is important for apatite formation in rare earth-CMAS systems while higher concentrations of Mg^{2+} in the reaction mixture have been suggested to push the equilibrium toward garnet formation. Interestingly, for the Gd+CMAS system apatite appears to be more stable than garnet even in MgO-rich systems, with the formation of Al^{3+} containing, Mg-RE apatite. Likewise, garnet is more stable in the Yb+CMAS system even for compositions containing CaO as the AE oxide. It is thus evident that in addition to the Ca:Si ratio in the coating-deposit reaction mixture, concentration of ions such Al^{3+} and Mg^{2+} as well as the identity of the rare earth ion play a pivotal role in silicate apatite and garnet stability and influence their equilibrium concentrations.

There is a growing interest in understanding the performance of multi-cation coating materials developed either using a "high entropy" approach, or designed to take advantage of more economical partially-refined RE oxide feedstock.[60–62] Results from this study demonstrate the significant influence of rare earth cation size on the identity, compositions, and relative phase fractions of the reaction products formed during coating-deposit interactions. In the case of multi-rare earth ion mixtures, it is likely that the formation of the resulting crystalline reaction products will be influenced by the average rare earth cation radius. Consequently, while designing the compositions of multi-cation coating materials, it will be crucial to determine whether the effective rare earth cation radius for the mixture increases or decreases the potential for formation of favorable reaction products.

5 | CONCLUSIONS

The Yb+CMAS and Gd+CMAS systems were studied to understand the stability and extent of the garnet phase at 1400°C. The conclusions are:

a. The rare earth (RE) ion radii are crucial in determining the stability of the silicate garnet phase. Yb^{3+} and Y^{3+} readily stabilize the phase, but silicate garnets weren't formed with Gd^{3+}, which is only ~3% larger than Y^{3+} (CN = 8). However, the radii appear less important in determining the stable composition range, with only a slight increase in the extent of the garnet solid solution field in Yb+CMAS as compared to the Y+CMAS system.
b. The RE ions play an important role in stabilizing garnet phase; in all cases the RE cations fill at least 67% of the dodecahedral sites, comprising at least 25% of the total cations in the phase.
c. Mg^{2+} shows a preference for the octahedral site over the dodecahedral site in the garnet crystal structure. For both the Yb-and Y-based garnets, the Mg^{2+} solubility limit in the octahedral site exceeds 90% of the available sites. The maximum Mg^{2+} solubilities in the dodecahedral sites increase slightly from ~25% of the sites (9 cat% total) in the Y+CMAS garnets to ~32% of the sites (11.9 cat% total) in the Yb+CMAS garnets.
d. The maximum silica solubility in Yb+CMAS garnets (33 cat%, as compared to the 27% in Y+CMAS garnet), is attained in compositions where Mg^{2+} is the only AE ion and is attributed to the increased Mg^{2+} solubility in the dodecahedral site.
e. The increasing RE ionic radii (from Yb^{3+} to Y^{3+} to Gd^{3+}) shift the equilibrium from garnet toward apatite for samples with equivalent Ca:Si ratio. For Y+CMAS, which is the only system that formed both garnet and apatite for the compositions studied, garnet formation was favored with higher Al^{3+} content and increasing Ca:Si ratio in the sample.

ACKNOWLEDGMENTS

Research supported by an Office of Naval Research supported collaboration with QuesTek Innovations, managed by Dr. David Shifler (N00014-17-C-2034). This work utilized shared equipment supported by NSF MRI DMR-1229263 (Hitachi SU8230), NSF EAR-1625422 (EPMA). The NSF MRSEC (DMR-2011401) and NNCI (ECCS-2025124) support of the UMN Characterization Facility, a member of the Materials Research Facilities Network (www.mrfn.org). The authors are grateful to Drs. Carlos Levi (UCSB), Dana Frankel and Pin Lu (QuesTek Innovations LLC), and Weiwei Zhang (Thermo-Calc Software) for the insightful discussions, and to Nikhil Karthikeyan for assistance with sample preparation.

NOTE ABOUT SUPPLEMENTARY INFORMATION

Complete tabulated phase lists and compositions for the Yb+CMAS and Gd+CMAS systems are reported in Table S1 and S2, respectively. Micrographs at several magnifications for all compositions studied in the Yb+CMAS and Gd+CMAS systems are in Table S3. Micrographs showing the evolution of microstructures of composition Gd-(0,0,0) at 1400°C between 25 and 500 h dwell times are shown in Figure S4.

ORCID

Eeshani Godbole https://orcid.org/0000-0002-2685-0041
Anette von der Handt https://orcid.org/0000-0003-1975-9909
David Poerschke https://orcid.org/0000-0002-6206-235X

REFERENCES

1. Stott FH, de Wet DJ, Taylor R Degradation of thermal-barrier coatings at very high temperatures. MRS Bulletin. 1994;19(10):46–49. http://doi.org/10.1557/s0883769400048223
2. Clarke DR, Levi CG. Materials design for the next generation thermal barrier coatings. Annu Rev Mater Res 2003;33:383–417.
3. Krämer S, Faulhaber S, Chambers M, Clarke DR, Levi CG, Hutchinson JW, et al. Mechanisms of cracking and delamination within thick thermal barrier systems in aero-engines subject to calcium-magnesium-alumino-silicate (CMAS) penetration. Mater Sci Eng A 2008;490:26–35.
4. Levi CG, Hutchinson JW, Vidal-Sétif M-H, Johnson CA Environmental degradation of thermal-barrier coatings by molten deposits. MRS Bulletin. 2012;37(10):932–941. http://doi.org/10.1557/mrs.2012.230
5. Naraparaju R, Schulz U, Mechnich P, Döbber P, Seidel F. Degradation study of 7 wt.% yttria stabilised zirconia (7YSZ) thermal barrier coatings on aero-engine combustion chamber parts due to infiltration by different $CaO–MgO–Al_2O_3–SiO_2$ variants. Surface and Coatings Technology 2014;260:73–81.
6. Poerschke DL, Jackson RW, Levi CG. Silicate deposit degradation of engineered coatings in gas turbines: progress toward models and materials solutions. Annu Rev Mater Res 2017;47:297–330.
7. Krämer S, Yang J, Levi CG. Infiltration-inhibiting reaction of gadolinium zirconate thermal barrier coatings with CMAS melts. J Am Ceram Soc 2008;91:576-83.
8. Zhao H, Richards BT, Levi CG, Wadley HNG. Molten silicate reactions with plasma sprayed ytterbium silicate coatings. Surface and Coatings Technology 2016;288:151-62.
9. Grant KM, Krämer S, Seward GGE, Levi CG. Calcium-magnesium alumino-silicate interaction with yttrium monosilicate environmental barrier coatings. J Am Ceram Soc 2010;93:3504-11.
10. Gledhill AD, Reddy KM, Drexler JM, Shinoda K, Sampath S, Padture NP. Mitigation of damage from molten fly ash to air-plasma-sprayed thermal barrier coatings. Mater Sci Eng A 2011;528:7214-21.
11. Mechnich P, Braue W. Volcanic ash-induced decomposition of EB-PVD $Gd_2Zr_2O_7$. Thermal barrier coatings to Gd-Oxyapatite, Zircon, and Gd,Fe-Zirconolite. J Am Ceram Soc 2013;96:1958-65.

12. Poerschke DL, Levi CG. Effects of cation substitution and temperature on the interaction between thermal barrier oxides and molten CMAS. J Eur Ceram Soc 2015;35:681-91.
13. Poerschke DL, Barth TL, Fabrichnaya O, Levi CG Phase equilibria and crystal chemistry in the calcia–silica–yttria system. Journal of the European Ceramic Society. 2016;36(7):1743–1754. http://doi.org/10.1016/j.jeurceramsoc.2016.01.046
14. Poerschke DL, Barth TL, Levi CG Equilibrium relationships between thermal barrier oxides and silicate melts. Acta Materialia. 2016;120:302–314. http://doi.org/10.1016/j.actamat.2016.08.077
15. Poerschke DL, Levi CG Phase equilibria in the calcia-gadolinia-silica system. Journal of Alloys and Compounds. 2017;695:1397–1404. http://doi.org/10.1016/j.jallcom.2016.10.263
16. Costa G, Harder BJ, Bansal NP, Kowalski BA, Stokes JL Thermochemistry of calcium rare-earth silicate oxyapatites. Journal of the American Ceramic Society. 2020;103(2):1446–1453. http://doi.org/10.1111/jace.16816
17. Wiesner VL, Harder BJ, Bansal NP. High-temperature interactions of desert sand CMAS glass with yttrium disilicate environmental barrier coating material. Ceram Int 2018;44:22738-43.
18. Stokes JL, Harder BJ, Wiesner VL, Wolfe DE. Effects of crystal structure and cation size on molten silicate reactivity with environmental barrier coating materials. Journal of the American Ceramic Society 2020;103(1):622-34.
19. Turcer LR, Krause AR, Garces HF, Zhang L, Padture NP. Environmental-barrier coating ceramics for resistance against attack by molten calcia-magnesia-aluminosilicate (CMAS) glass: Part I, $YAlO_3$ and γ-$Y_2Si_2O_7$. J Eur Ceram Soc 2018;38:3905-13.
20. Summers WD, Poerschke DL, Taylor AA, Ericks AR, Levi CG, Zok FW Reactions of molten silicate deposits with yttrium monosilicate. Journal of the American Ceramic Society. 2020;103(4):2919–2932. http://doi.org/10.1111/jace.16972
21. Stokes JL, Harder BJ, Wiesner VL, Wolfe DE. High-Temperature thermochemical interactions of molten silicates with $Yb_2Si_2O_7$ and $Y_2Si_2O_7$ environmental barrier coating materials. J Eur Ceram Soc 2019;39:5059-67.
22. Abdul-Jabbar NM, Fernandez AN, Jackson RW, Park D, Summers WD, Levi CG. Interactions between zirconia–yttria–tantala thermal barrier oxides and silicate melts. Acta Materialia 2020;185:171-80.
23. Godbole E, Karthikeyan N, Poerschke D. Garnet stability in the Al–Ca–Mg–Si–Y–O system with implications for reactions between TBCs, EBCs, and silicate deposits. J Am Ceram Soc 2020;103:5270-82.
24. Chavez JJG, Naraparaju R, Mikulla C, Mechnich P, Kelm K, Ramana CV, et al. Comparative study of EB-PVD gadolinium-zirconate and yttria-rich zirconia coatings performance against Fe-containing calcium-magnesium-aluminosilicate (CMAS) infiltration. Corros Sci 2021;190:109660.
25. Braue W, Mechnich P. Recession of an EB-PVD YSZ coated turbine blade by $CaSO_4$ and Fe, Ti-rich CMAS-type deposits. J Am Ceram Soc 2011;94:4483-9.
26. Eils NK, Mechnich P, Braue W. Effect of CMAS deposits on MOCVD coatings in the system Y_2O_3-ZrO_2: phase relationships. J Am Ceram Soc 2013;96:3333-40.
27. Krause AR, Garces HF, Senturk BS, Padture NP. $2ZrO_2{\cdot}Y_2O_3$ thermal barrier coatings resistant to degradation by molten CMAS: Part II, interactions with sand and fly ash. J Am Ceram Soc 2014;97:3950-7.
28. Mechnich P, Braue W. Solid-state CMAS corrosion of an EB-PVD YSZ coated turbine blade: Zr^{4+} partitioning and phase evolution. J Am Ceram Soc 2015;98:296–302.
29. Poerschke DL, Hass DD, Eustis S, Seward GGE, Van Sluytman JS, Levi CG. Stability and CMAS resistance of ytterbium-silicate/hafnate EBCs/TBC for SiC composites. J Am Ceram Soc 2015;98:278-86.
30. Poerschke DL, Seward GGE, Levi CG. Influence of Yb:Hf ratio on ytterbium hafnate/molten silicate (CMAS) reactivity. J Am Ceram Soc 2016;99:651-9.
31. Krause AR, Garces HF, Herrmann CE, Padture NP. Resistance of $2ZrO_2{\cdot}Y_2O_3$ top coat in thermal/environmental barrier coatings to calcia-magnesia-aluminosilicate attack at 1500°C. J Am Ceram Soc 2017;100:3175-87.
32. Qu Z, Sparks TD, Pan W, Clarke DR. Thermal conductivity of the gadolinium calcium silicate apatites: effect of different point defect types. Acta Materialia 2011;59(10):3841-50.
33. Schmitt MP, Stokes JL, Rai AK, Schwartz AJ, Wolfe DE. Durable aluminate toughened zirconate composite thermal barrier coating (TBC) materials for high temperature operation. J Am Ceram Soc 2019;102:4781-93.
34. Jackson RW, Zaleski EM, Hazel BT, Begley MR, Levi CG. Response of molten silicate infiltrated $Gd_2Zr_2O_7$ thermal barrier coatings to temperature gradients. Acta Materialia 2017;132:538-49.
35. Crum J V., Chong S, Peterson JA, Riley BJ. Syntheses, crystal structures, and comparisons of rare-earth oxyapatites $Ca_2RE_8(SiO_4)_6O_2$ (RE = La, Nd, Sm, Eu, or Yb) and $NaLa_9(SiO_4)_6O_2$. Acta Crystallographica Section E Crystallographic Communications 2019;75(7):1020-25.
36. Thomas S, Sebastian M. Silicate and aluminate based dielectric ceramics for microwave communication (Doctoral dissertation, National Institute for Interdisciplinary Science and Technology). 2010.
37. George NC, Denault KA, Seshadri R. Phosphors for solid-state white lighting. Annual Review of Materials Research 2013;43(1):481–501.
38. Smet PF, Parmentier AB, Poelman D. Selecting conversion phosphors for white light-emitting diodes. J Electrochem Soc 2011;158:R37.
39. Bachmann V, Ronda C, Meijerink A. Temperature quenching of yellow Ce^{3+} luminescence in YAG:Ce. Chemistry of Materials 2009;21(10):2077-84.
40. Haselton HT, Westrum EF. Low-temperature heat capacities of synthetic pyrope, grossular, and $pyrope_{60}grossular_{40}$. Geochimica et Cosmochimica Acta 1980;44(5):701-9.
41. Haselton HT, Newton RC. Thermodynamics of pyrope-grossular garnets and their stabilities at high temperatures and high pressures. J Geophys Res 1980;85:6973.
42. Toropov N. A., Bondar' I. A. Rare-earth silicates. Bulletin of the Academy of Sciences of the USSR Division of Chemical Science. 1960;9(2):145–148. http://doi.org/10.1007/bf00942881
43. Risbud AS, Helean KB, Wilding MC, Lu P, Navrotsky A. Enthalpies of formation of lanthanide oxyapatite phases. Journal of Materials Research 2001;16(10):2780-83.
44. Felsche J. Rare earth silicates with the apatite structure. Journal of Solid State Chemistry 1972;5(2):266-75.

45. Zhang H, Lu J, Shan X, Wu D, Zhao X, Guo F, et al. A promising molten silicate resistant material: rare-earth oxyapatite $RE_{9.33}(SiO_4)_6O_2$ (RE = Gd, Nd or La). J Eur Ceram Soc 2020;40:4101-10.
46. Mao H, Selleby M, Fabrichnaya O. Thermodynamic reassessment of the Y_2O_3–Al_2O_3–SiO_2 system and its subsystems. Calphad 2008;32(2):399–412.
47. Bondar' IA, Toropov NA. Phase equilibria in the ytterbium oxide-alumina system and their comparison with equilibria in other systems Ln_2O_3-Al_2O_3. Bulletin of the Academy of Sciences, USSR Division of Chemical Science 1966;15(2):195-99. https://doi.org/10.1007/BF00856037
48. Petrosyan AG, Popova VF, Gusarov VV, Shirinyan GO, Pedrini C, Lecoq P. The Lu_2O_3–Al_2O_3 system: relationships for equilibrium-phase and supercooled states. Journal of Crystal Growth 2006;293(1):74-7.
49. Fabrichnaya O, Savinykh G, Schreiber G. Phase relations in the ZrO_2–La_2O_3–Y_2O_3–Al_2O_3 system: experimental studies and phase modelling. J Eur Ceram Soc 2013;33:37–49.
50. Schneider SJ, Roth RS, Waring JL. Solid state reactions involving oxides of trivalent cations. J Res Natl Bur Stand Sect A Phys Chem 1961;65A:345.
51. Klimm D, Ganschow S, Pajączkowska A, Lipińska L. On the solubility of Nd^{3+} in $Y_3Al_5O_{12}$. Journal of Alloys and Compounds 2007;436(1-2):204-8.
52. Fabrichnaya O, Savinykh G, Schreiber G, Seifert HJ. Phase relations in the ZrO_2–Nd_2O_3–Y_2O_3–Al_2O_3 system: experimental study and thermodynamic modeling. J Eur Ceram Soc 2012;32:3171-85.
53. Fabrichnaya O, Savinykh G, Zienert T, Schreiber G, Seifert HJ. Phase relations in the ZrO_2-Sm_2O_3-Y_2O_3-Al_2O_3 system: experimental investigation and thermodynamic modelling. Int J Mater Res 2012;103:1469-87.
54. Wu P, Pelton AD. Coupled thermodynamic-phase diagram assessment of the rare earth oxide-aluminium oxide binary systems. Journal of Alloys and Compounds 1992;179(1-2):259-87.
55. Kanke Y, Navrotsky A. A calorimetric study of the lanthanide aluminum oxides and the lanthanide gallium oxides: stability of the perovskites and the garnets. Journal of Solid State Chemistry 1998;141(2):424-36.
56. Lakiza SM, Tishchenko YS, Lopato LM. Projections of the liquidus and solidus surfaces of the Al_2O_3-HfO_2-Gd_2O_3 phase diagram. Powder Metallurgy and Metal Ceramics 2011;50(7-8):429-41.
57. Sebastian MT, Ubic R, Jantunen H. Other important materials. Microwave Mater Appl. 2017;267–344.
58. Massoni N, Hegron R, Campayo L. Reinvestigation of the crystal structure of $Ca_2Ce_8(SiO_4)_6O_2$ apatite by Rietveld refinement. Acta Crystallographica Section E Crystallographic Communications 2018;74(7):955-59.
59. Shannon RD. Revised effective ionic radii and systematic studies of interatomic distances in halides and chalcogenides. Acta Crystallographica Section A 1976;32(5):751-67.
60. Ku AY, Dosch C, Grossman TR, Herzog JL, Maricocchi AF, Polli D, et al. Addressing rare-earth element criticality: an example from the aviation industry. JOM 2014;66(11):2355-59.
61. Ridley M, Gaskins J, Hopkins P, Opila E. Tailoring thermal properties of multi-component rare earth monosilicates. Acta Materialia 2020;195:698–707.
62. Turcer LR, Sengupta A, Padture NP. Low thermal conductivity in high-entropy rare-earth pyrosilicate solid-solutions for thermal environmental barrier coatings. Scr Mater 2021;191:40-5.

SUPPORTING INFORMATION

Additional supporting information may be found in the online version of the article at the publisher's website.

How to cite this article: Godbole E, von der Handt A, Poerschke D. Apatite and garnet stability in the Al–Ca–Mg–Si–(Gd/Y/Yb)–O systems and implications for T/EBC: CMAS reactions. J Am Ceram Soc. 2022;105:1596–1609. https://doi.org/10.1111/jace.18179